Effect of CeO$_2$ on Electrochemical Corrosion Resistance of Ni–P–CeO$_2$ Composite Coatings Prepared by Submerged Jet Electrodeposition

Xia Jie[1], Zhang Hong-wen[2], Fu Xiu-qing[1,3,*], Lin Jin-ran[1], Duan Shuang-lu[1], Shen Mo-qi[1], Jiang min-jie[1]

[1] College of Engineering, Nanjing Agricultural University, Nanjing 210031, P. R. China;
[2] College of Mechanical and Electrical Engineering, Shihezi University, Shihezi 832003, P. R. China;
[3] Key laboratory of Intelligence Agricultural Equipment of Jiangsu Province, Nanjing 210031, P. R. China
[*]E-mail: fuxiuqing@njau.edu.cn;

A novel method of submerged jet electrodeposition with incorporation of CeO$_2$ nanoparticles (NPs) was applied to remodel Ni–P alloy coatings. Surface morphologies of the coating surface were characterized by scanning electron microscopy observations, the composition and phase structure were studied using energy dispersive spectroscopy and X-ray diffraction, and the corrosion resistance was analyzed by the polarization curves and electrochemical impedance spectroscopy. Experimental results confirmed successful deposition of a homogenous coating on the surface of the metal matrix and improvement of the corrosion resistance after incorporation of CeO$_2$ NPs. The composite coatings showed the smallest corrosion current and the largest polarization resistance when 1.0 g/L of CeO$_2$ NPs was added in the plating solution, revealing the greatest corrosion resistance. The underlying potential mechanism is that the introduction of the nano-CeO2 phase effectively reduces the adsorption of corrosive media and protects the insoluble corrosion products, thereby promoting the occurrence of uniform corrosion.

1. INTRODUCTION

In the field of engineering, wear and corrosion are the primary cause of failure of engineering parts [1]. Production machines are often damaged due to insufficient mechanical performance. Surface modification of a component by depositing an alloy film on the surface has become one of the most effective methods to solve the problem of wear and corrosion [2]. Ni–Co [3, 4], Ni–B [5, 6], Ni–P [7-9], Ni–W [10], and other nickel-based alloys have shown high microhardness, wear resistance, corrosion

resistance, thermal stability, and other exceptional mechanical properties. Among these materials, the Ni–P alloy has particularly high corrosion resistance [9]. However, with the improvement in the production level, pure alloy materials can no longer meet the performance requirements. In recent years, particle-reinforced metal matrix composites (MMC) have attracted much attention owing to their superior comprehensive properties [11]. It has been illustrated that incorporation of particles in the metal matrix can enhance its performance or obtain an entirely new property.

Among various preparation methods of MMC, electrodeposition has attracted wide attention as an efficient and convenient method. Since the invention of DC electrodeposition technology [12], researchers have continuously investigated nanoparticle deposition processes in order to bring about innovation. Jet electrodeposition [13], pulse electrodeposition [14, 15], magnetically assisted electrodeposition [16] and ultrasound assisted electrodeposition [17] have been developed to respond to the changing performance requirements of materials. Unfortunately, according to the existing research results, the electrodeposition process is mostly limited to DC electrodeposition or jet electrodeposition and their improved processes. Research on combining the characteristics of the two processes is yet to be reported.

Many studies have reported the embedding of ceramic particles in MMC as reinforced particles, such as Al_2O_3 [18], TiO_2 [19-21], solid lubricant PTFE [22], hexagonal BN [23], and conductive graphene particles [24]. Particles with different characteristics can enable the metal matrix to obtain different property enhancements. Some studies have researched CeO_2 nanoparticles (NPs) as a stable rare earth oxide with high-temperature wear resistance, high-temperature oxidation resistance, and corrosion resistance. Chen et al. [25] illustrated that the incorporation of CeO_2 NPs into a thin film of bis-amino silane of bis–[triethoxysilylpropyl]amine (BTSPA) could enhance corrosion protection for carbon steel. Han et al. [26] illustrated that CeO_2 could improve the corrosion resistance of the Ni–W coatings effectively at high temperature.

Considering the limited investigation on Ni–P–CeO_2 nanocomposite coatings and the common methods of conventional jet electrodeposition, we propose a submerged jet electrodeposition (SJED) method to prepare Ni–P–CeO_2 nanocomposite coatings. Further, the effects of the concentration of CeO_2 NPs in the plating solution are examined to establish the optimal preparation procedure. Moreover, the appearance, structure, and the electrochemical corrosion behavior of the composite coatings are investigated.

2. EXPERIMENTAL

2.1. Experimental principle

The conventional jet electrodeposition principle is shown in Figs. 1(a) and 2(a). The plating solution in the nozzle is sprayed on the surface of the workpiece at a high speed. In the spray coverage area, the cathode workpiece and the anode nickel rod form a closed current loop through the plating solution. Deposition of metal ions is realized under the action of the external electric field, and it does not occur in the area where no current passes. During the electrodeposition process, the high-speed spraying solution has a mechanical activation effect on the coating, which greatly improves the deposition speed. However, the following problems might occur in conventional jet electrodeposition

because of the limited size of the nozzle orifice and the short distance between the nozzle and the workpiece surface:

(i)   Cellular bulges are easily produced on the coating surface because of point discharge shielding effects. With continued deposition, large cellular bulges grow at a faster rate and finally submerge smaller bulges, thereby forming pits between cellular bulges. This result seriously affects coating compactness, leading to the formation of large bumps that largely contribute to severe corrosion behavior [27];

(ii)   High-speed spraying of the plating solution causes high pressure on the workpiece and shedding of NPs that have been adsorbed on the surface of the cathode;

(iii)   The coating surface out of the spray area is exposed to air, and an oxidation film forms and adheres to the surface due to the spray area of the nozzle cannot cover the workpiece surface at one time; this further leads to delamination of the coating.

(a) conventional jet electrodeposition   (b) submerged jet electrodeposition
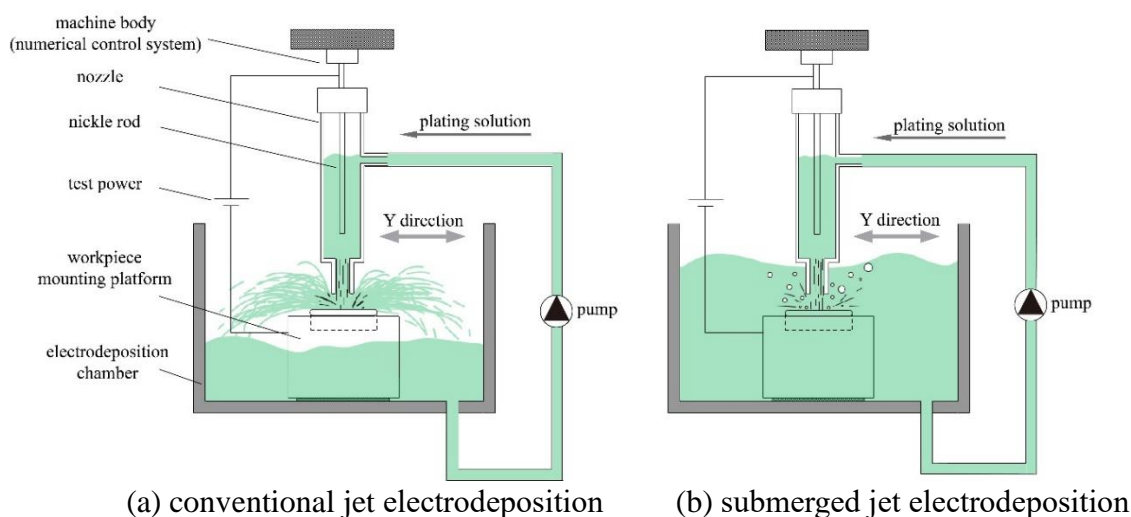
Figure 1. Comparison of the conventional and proposed electrodeposition methods.
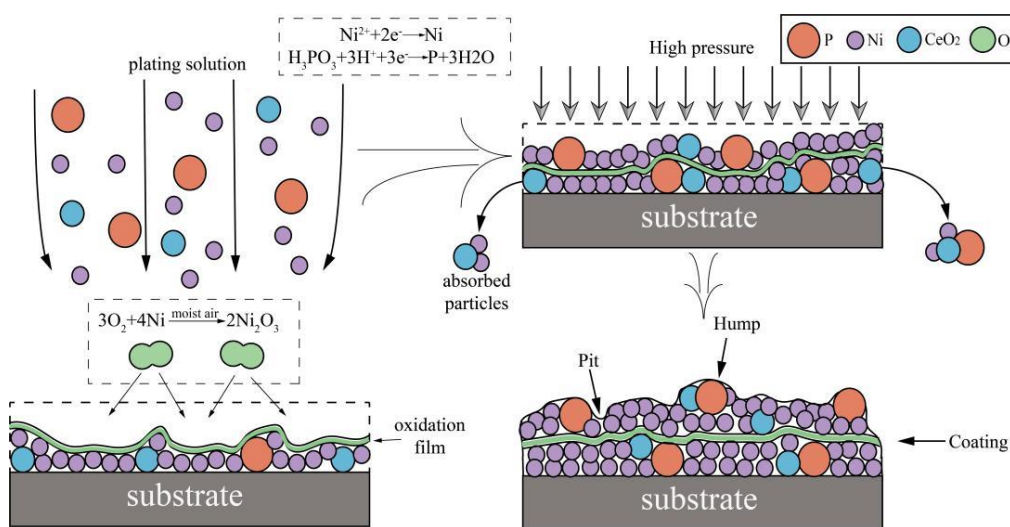
(a) Microprocess model of conventional jet electrodeposition.
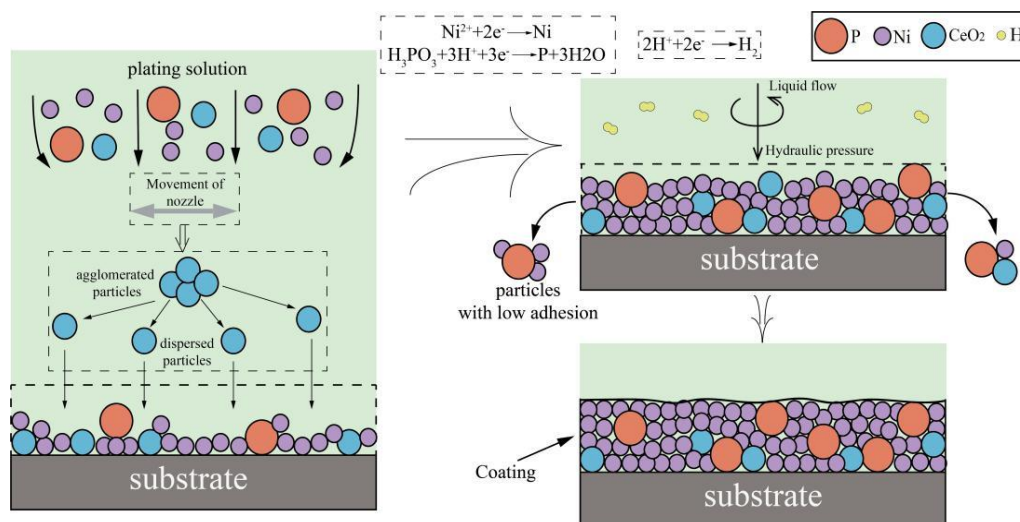
(b) Microprocess model of submerged jet electrodeposition.

Figure 2. Comparison of the models of the conventional and proposed electrodeposition microprocesses.

The principle of SJED is depicted in Figs. 1(b) and 2(b). The test power supply, nickel rod, and workpiece form a complete current loop through the plating solution. During the entire deposition process, the surface of the workpiece is absolutely exposed to the plating solution, thereby preventing the splashing of the plating solution and oxidation of the coating surface. This is advantageous for realizing a uniform distribution of metal crystals on the surface of the workpiece. Considering the large specific surface area of the NPs to be deposited, we improve the dispersion process of NPs by immersing the nozzle in the plating solution while spraying. Furthermore, under the combined action of pressure and liquid flow, hydrogen emitted from the cathode and the particles deposited with poor adhesion are continuously removed, thus optimizing the electrocrystallization environment and increasing the nucleation rate of electrocrystallization. At the same time, the circulation of the plating solution accelerates electromigration as well as the convection and diffusion of the metal ions. In addition, the concentration polarization phenomenon that occurs easily in conventional electrodeposition is avoided.

2.2. Experimental

In the experiment, the substrate was made of #45 steel with a size of 25 mm × 10 mm × 8 mm and the CeO_2 NPs had an average size of 100 nm and 99 wt.% purity. The plating solution composition and process parameters are listed in Table 1. For the pretreatment of the workpiece, it was mechanically polished with waterproof sandpapers of various meshes (320, 800, 1500) until specular reflection was achieved. Next, electro-clean liquid was used to degrease the surface of the workpiece, and a two-step (weak and strong) activation treatment was performed while rinsing the workpiece with deionized water after each step. On the pretreated workpieces, Ni–P–CeO_2 composite coatings were deposited with 0 g/L, 0.5 g/L, 1.0 g/L, and 1.5 g/L CeO_2 NP addition separately. After successful deposition, the coating surfaces were rinsed with deionized water and subjected to ethanol and ultrasonic cleaning.

Table 1. Composition of the plating solution and the respective process parameters for electrodeposition.

| Plating Solution Composition	Concentration (g/L)
Nickel sulfate hexahydrate	200
Nickel chloride hexahydrate	30
Phosphoric acid	20
Orthoboric acid	30
Citric acid	60
Thiourea	0.01
Sodium dodecyl sulfate	0.08
CeO2 NPs	0, 0.5, 1.0, 1.5
Process Parameters	
Current density (A/cm^2)	0.5
Temperature (°C)	60
PH	1. 0–1.5
Deposition time (min)	20
Moving speed (mm/min)	1500

2.3. Instruments

Scanning electron microscopy (SEM) (Quanta FEG250; FEI Instruments, Hillsboro, OR, USA) was performed to investigate the surface morphology before and after corrosion of the coatings. The composition of the coatings was analyzed by energy dispersive spectroscopy (EDS; XFlash 5030 Bruker AXS, Inc., Berlin, Germany), with point scanning and area scanning (1 mm^2) methods. The phase structure of the coatings was analyzed by X-ray diffraction (XRD; PANalytical X'pert; PANalytical Inc., Almelo, The Netherlands) spectroscopy with the spectrometer operated at 40 kV and 300 mA with Cu-Kα radiation (λ = 1.5406Å) and a scanning range of 20°–90°.

Electrochemical tests were performed in a three-electrode system using a CS350 electrochemical workstation (Wuhan Corrtest Instruments Corp., Ltd., Wuhan, China). The workpiece encapsulated with epoxy resin was immersed in 50 g/L NaCl corrosive medium without agitation to act as the working electrode; the reference electrode was a saturated calomel electrode (SCE), and the auxiliary electrode was a bright platinum piece. Polarization curve measurement by potentiodynamic sweeping (speed = 1 mV/s) and electrochemical impedance spectroscopy (EIS) were performed at room temperature. The polarization curve epitaxy method was used to characterize the corrosion potential and corrosion current, which are pivotal parameters for analyzing the corrosion resistance of the coatings. The EIS diagram of the coatings immersed in NaCl solution was completed under open circuit potential. The applied

frequency ranged from 10^5 Hz down to 10^{-2} Hz, and the scanning direction was from high frequency to low frequency. Further, ZsimpWin software was used for fitting the results for analysis.

3. RESULTS AND DISCUSSION

*3.1. Surface micromorphology and elemental concentration analysis*

(a) Ni–P　　　　　　　　　　　　　　(b) Ni–P–0.5g/LCeO$_2$

(c) Ni–P–1.0g/LCeO$_2$　　　　　　　　(d) Ni–P–1.5g/LCeO$_2$
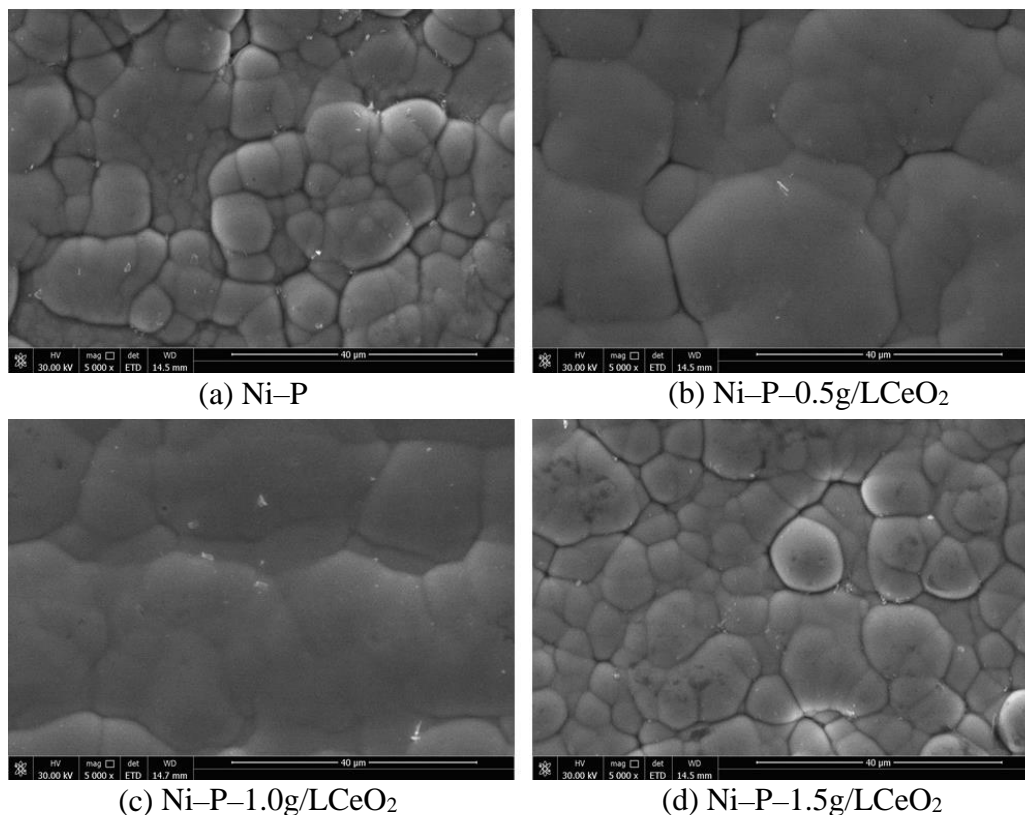
Figure 3. SEM images of the as-prepared Ni–P alloy coating, and Ni–P–CeO$_2$ composite coatings with increasing CeO$_2$ concentrations of 0.5, 1.0, and 1.5 g/L.

Fig. 3 shows the surface morphology of the Ni–P alloy coating and the Ni–P–CeO$_2$ composite coatings. As the figure shows, the coatings had homogenous structures with no obvious defects such as bumps and pits. The Ni–P alloy coating (Fig. 3(a)) had a rough surface comprising cells of different sizes and obvious boundaries and tiny pores. The cells were stacked on top of each other to form a circular island-like nodular structure. When 0.5 g/L CeO$_2$ NPs was added to the plating solution (Fig. 3(b)), the density of the coating significantly improved and the phenomenon of cell stacking disappeared. However, the size of cells varied greatly and there were still obvious boundaries. When 1.0 g/L of CeO2 NPs was added (Fig. 3(c)), the compactness and flatness of the coating further improved, the structure was more compact, the cells of uniform size were closely arranged, and the boundary was extremely fuzzy. As Fig. 3(d) shows, agglomeration of round or quasi-round particles appeared on the surface of the Ni–P–1.5g/LCeO$_2$ composite coating, and obvious protrusions were observed.

The change in the surface morphology of the coatings is affected by the uniformity of the nucleation of the cathode surface and the difference in the grain growth rate [28]. During the deposition

process, the submerged spray of the anode nozzle promotes dispersion of CeO_2 NPs and the migration of metal ions. CeO_2 NPs serve as an insulating material and thus do not provide favorable sites for the alloy nucleation to participate in the deposition process. However, the adsorption of ions in the ion layer promote the migration of metal cations to the cathode surface [29]. NPs that adsorb a large amount of cations adhere to the surface of the cathode and are captured and buried by the rapidly growing alloy coatings, thus acting as the crystallization nucleus of the alloy grains. As a result, a benign crystallization cycle is formed and the nucleation rate greatly improves. In the grain growth stage, the inert CeO_2 phase is a typical representative of high resistance and can be regarded as the dielectric phase in the coatings; it plays a shielding role and prevents the coarse growth of Ni grains [30]. Furthermore, the nanoscale size of CeO_2 particles can effectively fill the pores and microcracks on the surface of the coatings, thus promoting the formation of surfaces with more uniform physical and chemical properties. However, when the concentration of CeO_2 NPs is too large to be dispersed by the submerged spray, the balance of the crystallization cycle is broken. The agglomerated particles are likely to cause lattice disorder and negatively affect the surface morphology of the coatings [31].


(a) Analyzed surface (b) Ce element

(c) Ni element (d) P element
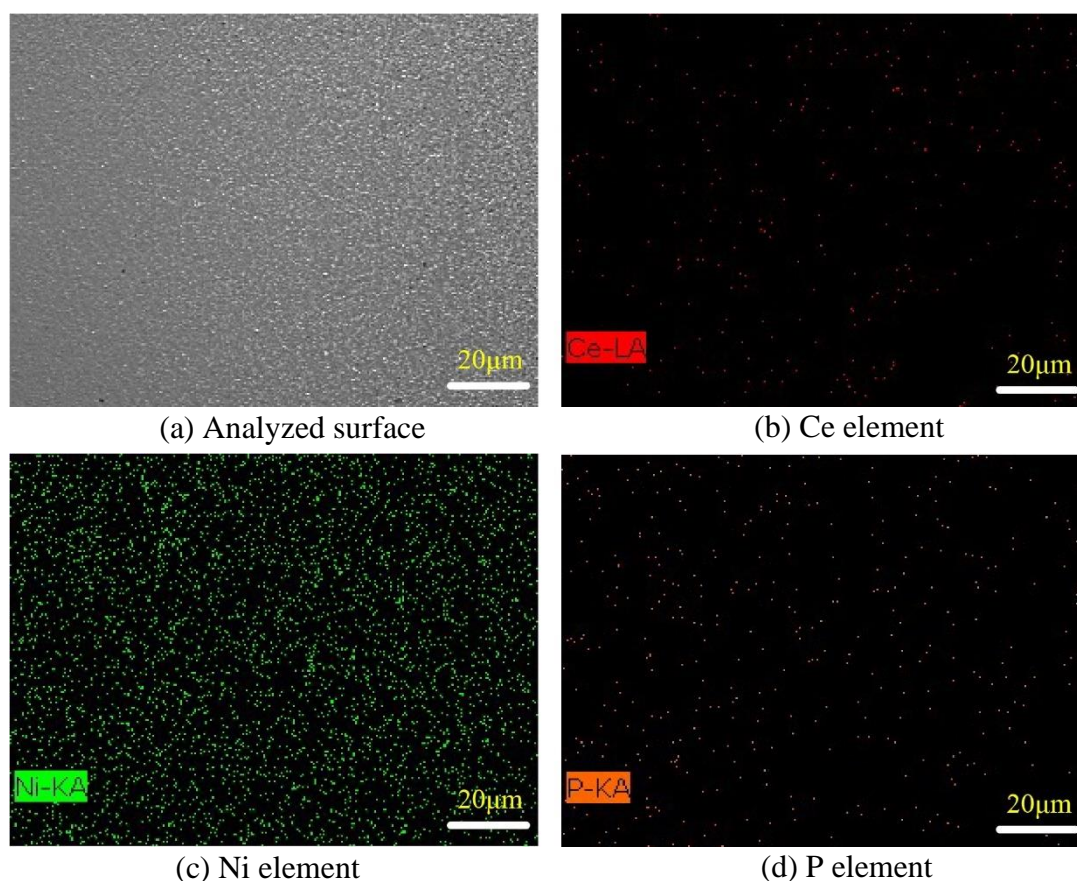
Figure 4. Element distribution map of Ni–P–1.0g/LCeO$_2$ composite coating: the SEM image of the analyzed surface, and Ce, Ni, P element.

The EDS mapping of the Ni–P–1.0g/LCeO$_2$ composite coating is shown in Fig. 4; it indicates the presence of Ni, P, and Ce elements in the composite coating and that CeO_2 NPs were successfully embedded in the alloy lattice and dispersed uniformly on the coating surface. No particle agglomeration

was observed, suggesting that SJED effectively promotes the dispersion of NPs in the plating solution. Relevant studies [1, 2] revealed that the uniform distribution of elements and particles is conducive to improving the corrosion resistance of coatings.
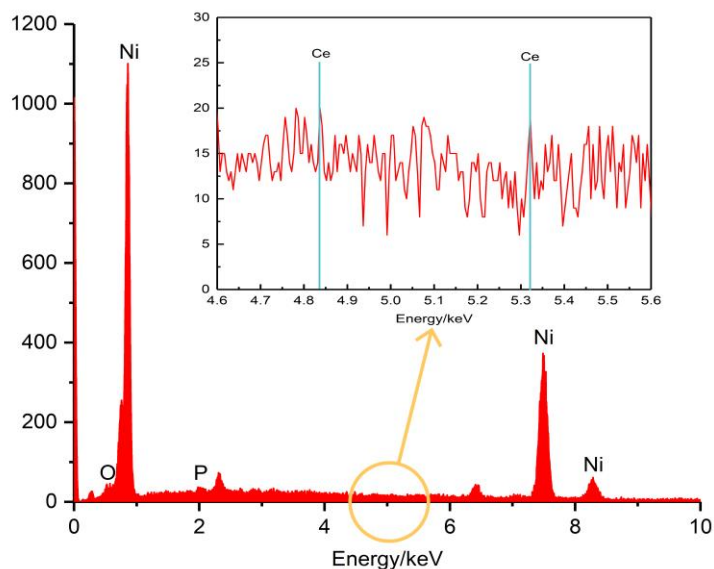
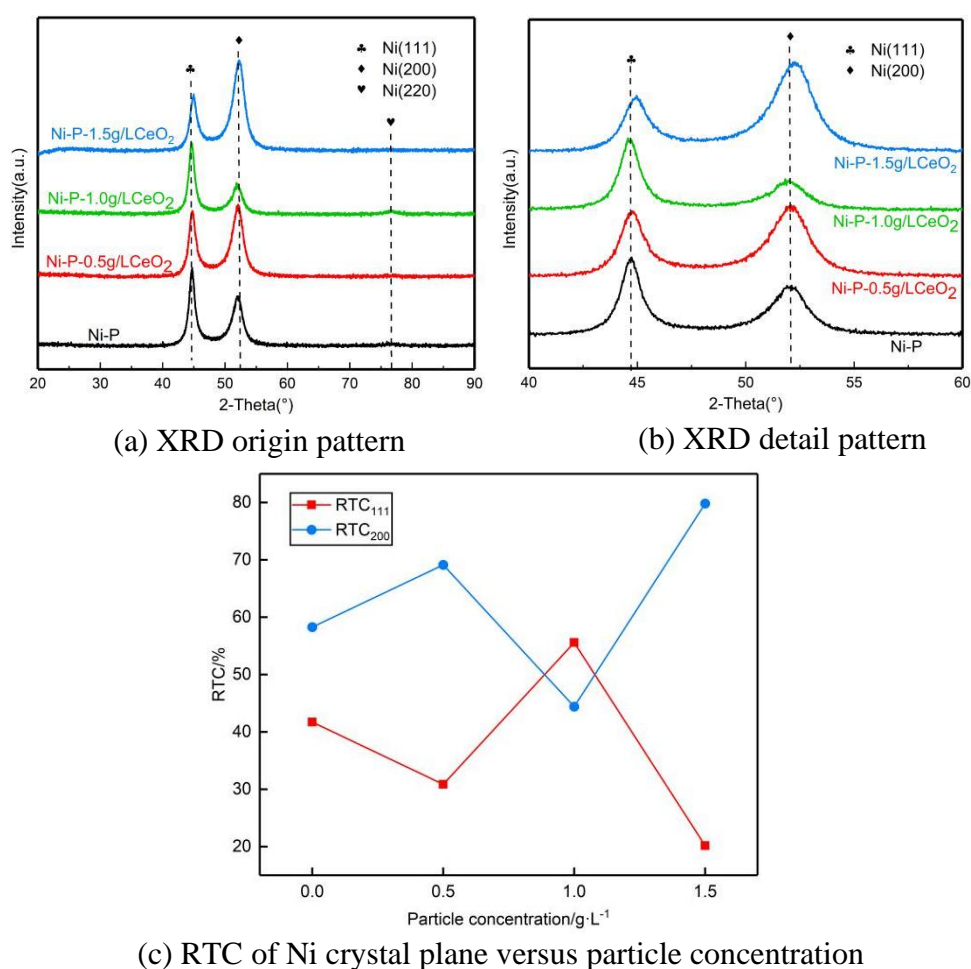**Figure 5.** EDS diagram of Ni–P–1.0g/LCeO$_2$ composite coating.
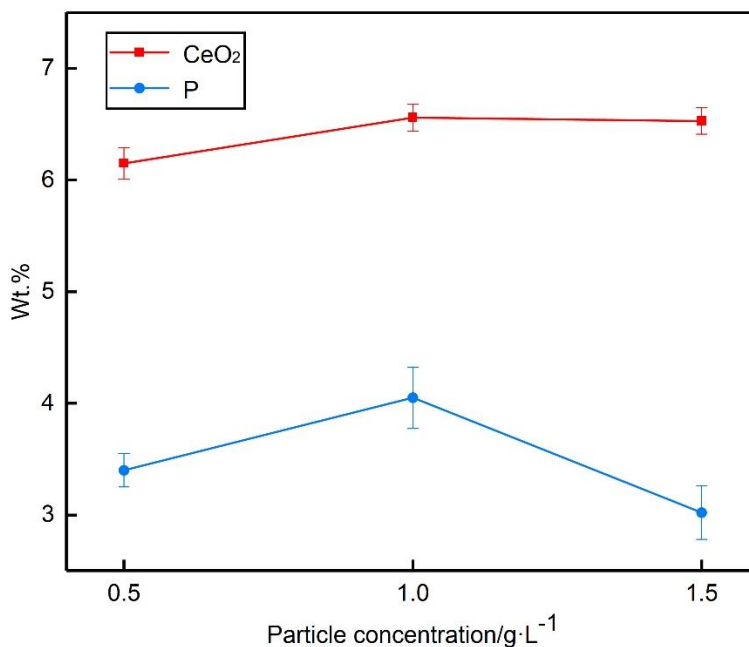
Figure 6. Weight percent of CeO$_2$ and P in the coatings versus particle concentration in the plating solutions.

The EDS point-scanning analysis results of the Ni–P–1.0g/LCeO$_2$ composite coating are shown in Fig. 5. Note that the peaks of element P are small and those of Ce are hard to observe even in the magnified diagram because Ni concentration was much higher than that of Ce and P in the plating solution. This result is consistent with the mass fractions shown in Fig. 6. The mass fraction of CeO$_2$ in the composite coating reached a state of saturation (6.56%) when the particle concentration was 1.0 g/L

in the plating solution. We speculate that the ion cloud formed by CeO_2 around itself in the deposition process is adsorbed on the cathode surface through troposphere and diffusion layers [31], but the actual number of CeO_2 NPs adsorbed on cathode electrode do not increase because the incorporation of inert CeO_2 reduces the conductivity of the electroplating solution and thus inhibits the formation of an ion cloud. The mass fraction of P increased first and then decreased, and when the concentration of CeO_2 NPs in the plating solution was 1.0 g/L, it reached the maximum, which was 19.1% higher than that at 0.5 g/L CeO_2. A study [32] suggested that the resistance of the coating increases with the increase of P concentration when the coating is corroded in neutral solution. Moreover, corrosion occurs first in the low-P-content area, which is mainly attributed to the effective inhibition of corrosive diffusion by the formation of the P-rich layer on the coating surface.

3.2. Phase analysis

(a) XRD origin pattern   (b) XRD detail pattern

(c) RTC of Ni crystal plane versus particle concentration

Figure 7. (a–b) XRD patterns of Ni–P and Ni–P–CeO_2 coatings; (c) effect of particle concentration in the plating solution on the RTC of Ni (111) and Ni (200).

      Figs. 7(a) and (b) show the XRD patterns of the coatings, where 2-Theta of 44.577°, 52.008°, and 76.797° correspond to the Ni (111), Ni (200), and Ni (220) crystal plane diffraction peaks, respectively. As there was no characteristic diffraction peak of P, it could be illustrated that Ni and P formed substitutional solid solution in the crystallization process [33]. As Fig. 7(b) shows, the diffraction

peak shifted slightly to the right when 1.5g/L CeO_2 was added. The interplanar spacing and lattice parameters were found to decrease according to the calculation based on the Bragg equation $\boldsymbol{2d\sin\theta = n\lambda}$ [34]. This can be ascribed to the increased residual stress in the coating caused by the addition of NPs. Compared with other major crystal planes, (111) and (200) crystal planes are significantly highly preferred orientations since their surface free energy is lower than that of other planes. The relative degree of orientation of preferred crystal planes is characterized by the relative texture coefficient (RTC), calculated as follows:

$$RTC_{(hkl)} = \frac{I_{(hkl)}/I_{0(hkl)}}{\sum(I_{(hkl)}/I_{0(hkl)})} \times 100\%$$

where $\boldsymbol{I_{(hkl)}}$ and $\boldsymbol{I_{0(hkl)}}$ represent the diffraction intensities of the deposit specimen and standard specimen (hkl) crystal planes [3]. The relationships between CeO_2 NPs concentration in the plating solution and RTC_{111} as well as RTC_{200} are shown in Fig. 7(c). The largest RTC_{111} and the smallest RTC_{200} were obtained when 1.0 g/L CeO_2 was added. The reason is that nickel atoms need higher surface energy to absorb and form nuclei on the (111) crystal plane because the (111) plane is more closely arranged than the (200) plane. By contrast, Ce atoms contain a large amount of effective charge and can absorb a large number of metal ions, thereby acting as a catalyst and reducing the surface energy when participating in deposition; thus, the driving force of grain growth changes and the nucleation rate of the (111) crystal plane increases [35]. When 1.5 g/L CeO_2 was added, NP aggregates easily covered the nucleation sites on the substrate, making Ni atoms difficult to be adsorbed to and grown on the (111) crystal plane. Larger RTC_{111} results in a denser microscopic plane of the coating on the level of cell size, which improves the anti-corrosion performance to some extent.

3.3. Corrosion behavior and mechanism analysis
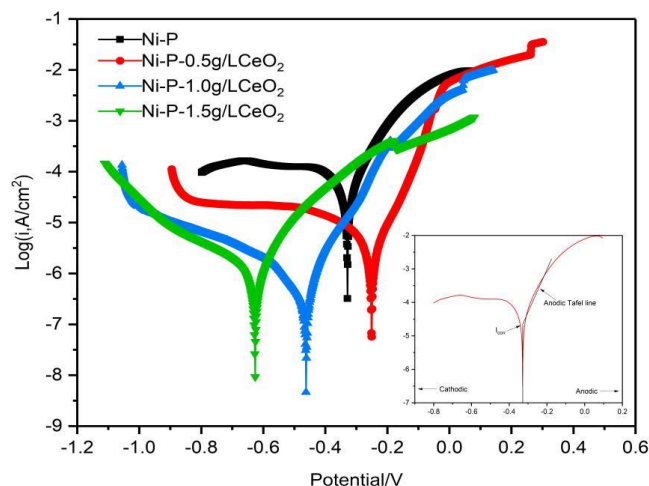
Figure 8. Polarization curves of the Ni–P alloy coating, and Ni–P–CeO_2 composite coatings with 0.5, 1.0, and 1.5 g/L NPs addition.

Table 2. The electrochemical parameters derived from polarization curves of the Ni–P coatings before and after addition of different concentrations of CeO_2 NPs.

Type of coatings	$E_{corr}(V)$	$I_{corr}(A/cm^2)$	$\beta_a(mV)$	$\beta_c(mV)$	$R_p(\Omega\ cm^2)$
Ni–P	-0.328	4.18×10^{-5}	255	-97	5.40×10^2
Ni–P–0.5g/LCeO$_2$	-0.251	3.92×10^{-6}	98	-241	7.25×10^3
Ni–P–1.0g/LCeO$_2$	-0.462	6.40×10^{-7}	96	-296	4.71×10^4
Ni–P–1.5g/LCeO$_2$	-0.627	1.53×10^{-6}	142	-375	2.94×10^4

The corrosion resistance of the coatings was investigated by the polarization curve (Fig. 8). The transient process of spontaneous passivation shown in the anodic polarization curve reveals that the coatings prepared by the new process had strong corrosion resistance. Table 2 shows the electrochemical parameters fitted by the extrapolation of the polarization curves and polarization resistance (R_p) calculated by Stern's formula. The results indicate that the corrosion current density decreased substantially while polarization resistance increased sharply with the addition of CeO_2 NPs, and both parameters showed a change of above an order of magnitude. The reason for this is that CeO_2 codeposition fills boundaries and pores of some cells, reducing the active corrosion sites of Cl^-. It is easy for corrosive Cl^- to induce local corrosion on the coating surface in the corrosion process, while numerous corrosion micro-batteries formed by CeO_2 NPs diffuse in the coating, promoting anode polarization and inhibiting the local corrosion caused by crystal defects on the coating surface, and thus facilitating uniform corrosion [36]. The experimental results suggest that Ni–P coating had localized corrosion on its surface, and a slightly spontaneous passivation occurred on the composite coatings embedded with CeO_2 NPs.

According to Table 2, with the continuous addition of CeO_2 NPs in the composite coatings, the corrosion current density decreased first and then increased, while the polarization resistance showed the opposite trend. The composite coating exhibited the optimal corrosion resistance when the CeO_2 concentration was 1.0 g/L, with I_{corr} of 6.4×10^{-7} A/cm^2 and R_p of 4.7×10^4 kΩ cm^2. This is because the gradual change of metal crystal orientation with increasing CeO_2 concentration leads to the enhancement of coating's immunity against Cl^- by reducing the active sites on this surface that could be specifically absorbed by Cl^-, given that CeO_2 and Ni grains have similar lattice types [35]. In addition, R_p of metal coated with a passive film depends on the dissolution of the film, which is well protected by inert CeO_2 NPs. The increased I_{corr} of composite coating Ni–P–1.5g/LCeO$_2$ can be attributed to the chemical heterogeneity caused by non-uniform distribution of agglomerated NPs in the metal matrix [37].

The coatings were evaluated by EIS diagrams to further study the corrosion resistance. The Nyquist plots shown in Fig. 9 suggests that the capacitance arcs represented by the four test curves had a large size, indicating good corrosion resistance of the coatings. The capacitance arc of the coatings had a larger size in the entire frequency range when CeO_2 NPs were added; this is in good agreement with the result observed in the polarization curves. The reason for this trend is that inert CeO_2 acts as a dielectric phase, i.e., a barrier between the electrolyte and electrode interface [38]; thus, the current interaction is effectively prevented during the corrosion process.
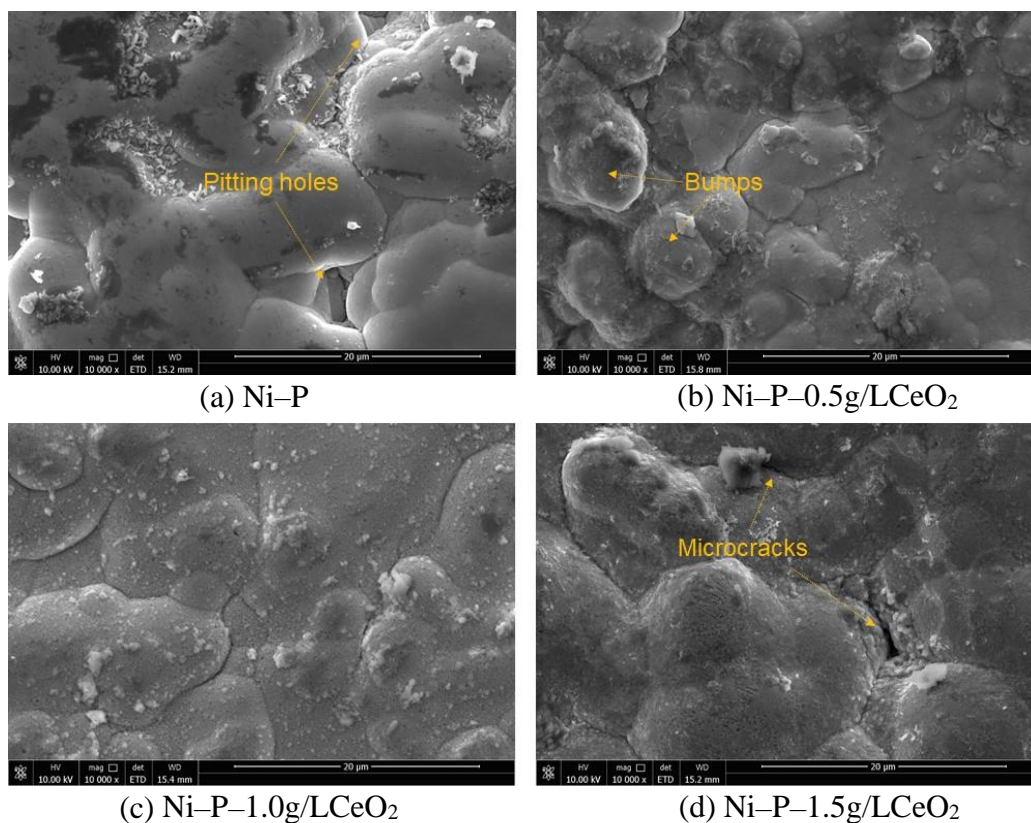
(a) Ni–P
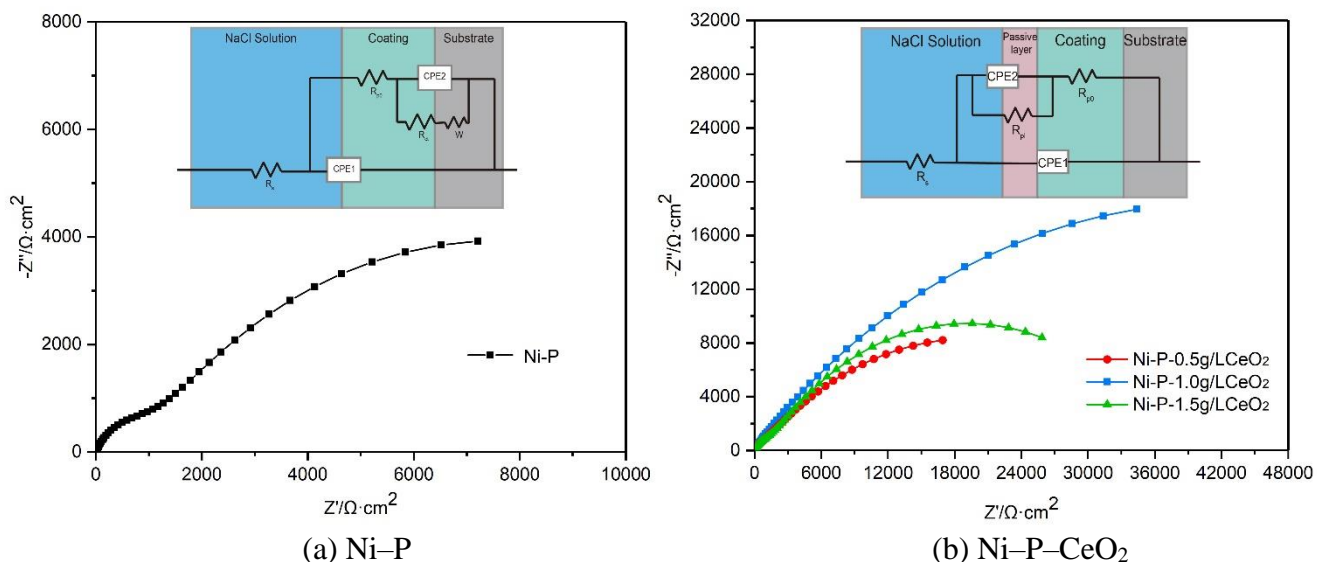
(b) Ni–P–CeO₂

Figure 9. Nyquist plots and corresponding equivalent electrical circuits (EEC) used to simulate experimental data of the Ni–P alloy coating, and Ni–P–CeO$_2$ composite coatings with 0.5, 1.0, and 1.5 g/L NPs addition.

Because EIS analysis results of Ni–P coating are in line with the results reported by Yusuf et al. [39], our results were fitted with the EEC model shown in Fig. 9(a), where R_s represents the electrolyte resistance, R_{p0} is the pore resistance of the coatings, R_{ct} stands for the charge transfer resistance of the substrate/coating interface, CPE1 and CPE2 are two constant phase angle elements corresponding to the high-frequency and low-frequency electric double-layer capacitors, respectively. In addition, considering the existence of an open and approximately straight line at low frequency, we introduced Warburg diffusion impedance, which was parallel to CPE2 and formed during mass transfer control. In view of slight spontaneous passivation of the composite coating embedded with CeO$_2$ NPs in the corrosive media, the electrochemical interface of the system was defined as electrolyte solution/passivation layer/nickel-based coating. The composite coatings showed similar EIS diagrams, and the diagram was fitted with the EEC model as shown in Fig. 9(b). The model contained two time constants: one time constant composed of CPE1 and R_{p0} in the high frequency was used to characterize the intrinsic properties of the nickel-based coating, while the other time constant comprising CPE2 and resistance of the passivation layer R_{pl} in the low frequency was controlled by the charge-transfer process, and it was used to characterize the intrinsic properties of the passivation layer [30].

The fitting results are shown in Table 3. The Ni–P coating had a low R_{p0} of 569 Ω cm^2, indicating high porosity of the coating and increased activity of corrosive media in the corrosion process. In addition, unstable corrosion products gathered at defects easily. In comparison, the composite coatings had higher R_{p0}, so they were more immune to the corrosion behavior. It is worth noting that the R_{pl} first increased and then decreased with the addition of CeO$_2$ NPs, verifying the super high corrosion resistance of the Ni–P–1.0g/LCeO$_2$ composite coating. The passivation layer served as a barrier against the corrosive medium and prevented oxygen transfer in the corrosion process, thereby blocking electronic transmission of chemical reactions and effectively protecting the coating [40].

Table 3. Fitting results of impedance spectra for the Ni–P coatings before and after addition of different concentrations of CeO_2 NPs.

Type of coatings	R_{p0} (Ω cm²)	CPE1 Y_0 (Ω^{-1} s^n cm^{-2})	n1	R_{ct} (Ω cm²)	R_{pl} (Ω cm²)	CPE2 Y_0 (Ω^{-1} s^n cm^{-2})	n2	W (Ω cm² s$^{0.5}$)
Ni–P	569	4.447×10^{-5}	0.8604	750.6	-	103.9×10^{-5}	0.9085	3.643×10^{-3}
Ni–P–0.5g/LCeO$_2$	1505	7.050×10^{-5}	0.7943	-	1.278×10^{4}	43.21×10^{-5}	0.6713	-
Ni–P–1.0g/LCeO$_2$	2132	6.902×10^{-5}	0.7403	-	8.372×10^{4}	7.297×10^{-5}	0.6001	-
Ni–P–1.5g/LCeO$_2$	1222	2.277×10^{-5}	0.8182	-	3.504×10^{4}	13.54×10^{-5}	0.5080	-

(a) Ni–P

(b) Ni–P–0.5g/LCeO$_2$

(c) Ni–P–1.0g/LCeO$_2$

(d) Ni–P–1.5g/LCeO$_2$

Figure 10. SEM images of the corroded Ni–P alloy coating, and Ni–P–CeO$_2$ composite coatings with increasing CeO$_2$ concentrations of 0.5, 1.0, and 1.5 g/L.

The surface morphology of the coatings which had been tested by the potentiodynamic sweeping and EIS experiments was observed after immersion in 50g/L NaCl solution for 4 days. A number of corrosion product aggregations could be seen in the SEM images. The Ni–P coating was the most seriously corroded (Fig. 10(a)), and there were some pitting holes and cracks on its surface, confirming the previous speculation. Corrosive Cl⁻ ions are easily adsorbed on the physical defects on the coating surface, and the metal attached to them dissolves to form soluble chloride. In this case, active dissolution sites, namely pitting nuclei, are formed on the coating surface. The pitting nuclei grow continuously and

develop into macro pitting holes under the circumstance of metal potential exceeding the pitting potential. Under the action of the anode current, Cl$^-$ ions move to and enrich the pitting holes, and the material transfer inside and outside the hole is greatly hindered due to the geometry and covering of corrosion products, leading to the formation of concentration cells and aggravation of corrosion. Wang et al. [27] suggested grain boundary density to be an important factor affecting the corrosion resistance. Grain boundary is prone to corrosion because its energy level is higher than intercrystalline energy level. As shown in Fig. 4(a), the Ni–P coating had a higher grain boundary density, so it was easily corroded by Cl$^-$ ions, and corrosion sites developed into cracks with progressing corrosion time.

The CeO$_2$-embedded coating showed no pitting holes on the surface, indicating that CeO$_2$ NPs alleviate the corrosion of the coating. When the concentration of CeO$_2$ NPs was 1 g/L (Fig. 10(c)), the coating surface corroded uniformly but mostly slightly. On the one hand, CeO$_2$ NPs are adsorbed as the inert rare earth composite and uniformly distribute on the coating surface to fill the pores and microcracks. On the other hand, CeO$_2$ NPs function as active oxide that accelerates the passivation of the anode during the corrosion process [41], transforming the corrosion mechanism from pitting corrosion to uniform corrosion. The coating surface showed poor overall flatness, with microcracks and bumps observed when the concentration of CeO$_2$ NPs was 0.5 g/L (Fig. 10(b)) and 1.5 g/L (Fig. 10(d)). The reason is that black corrosion products easily aggregate because a low concentration of CeO$_2$ NPs cannot stabilize the corrosion products and make them protective [42]. The cracks on the surface suggest the occurrence of stress corrosion cracking when a metal is generally passivated. Considering the selectivity feature of chemical adsorption, Cl$^-$ ions are adsorbed to the transition metal Ni prior to oxygen, resulting in local breakage of the passivation film and the formation of the crack core. The stress produced by residual hydrogen in the coating provides a preferred path for the high-speed dissolution of the crack tip while the crack wall remains passivated, thus forming surface cracks [6].

4. CONCLUSIONS

(1)   Coatings prepared by SJED showed excellent surface morphology. The Ni–P–CeO$_2$ composite coating showed a more uniform and compact microstructure than Ni–P alloy coating. The addition of 1.0g/L CeO$_2$ NPs was the most prominent. Ni–P–1.0g/LCeO$_2$ composite coating also exhibited the largest RTC$_{111}$ and mass fraction of CeO$_2$ and P.

(2)   The incorporation of CeO$_2$ decreased I$_{corr}$ and increased R$_p$ during the corrosion process. The composite coatings showed a large size of capacitance arcs, from which the maximum R$_{p0}$ and R$_{pl}$ were fitted for a CeO$_2$ concentration of 1.0 g/L.

(3)   Ni–P–1.0g/LCeO$_2$ composite coating, which resulted in no obvious bumps and microcracks on the coating surface after corrosion, had the strongest immunity to the corrosive media. It could be seen that CeO$_2$ stabilized the corrosion products and transformed the corrosion mechanism from pitting corrosion to uniform corrosion.

(4)   The submerged jet electrodeposited Ni–P–1.0g/LCeO$_2$ nanocomposites owns excellent corrosion resistance, which can be used as a protective medium for metal matrix in a corrosive working

environment. And the corrosive environment discussed in this paper is neutral, strong acid and alkaline environments need to be further explored.

References

1. W. Zhang, B. Li and C. Ji, *Ceram. Int.*, 45 (2019) 14015.
2. X. Fu, W. Ma, S. Duan, Q. Wang and J. Lin, *Materials (Basel)*, 12 (2019).
3. P. Hasanpour, P. Salehikahrizsangi, K. Raeissi, M. Santamaria, L. Calabrese and E. Proverbio, *Surf. Coat. Technol.*, 368 (2019) 147.
4. Y. Li, L. Shan, Y. Sui, J. Qi, F. Wei, Y. He, Q. Meng, Y. Ren and J. Liu, *Journal of Materials Science: Materials in Electronics*, 30 (2019) 13360.
5. R. Offoiach, M. Lekka, A. Lanzutti, V. Martínez-Nogués, J. M. Vega, E. García-Lecina and L. Fedrizzi, *Surf. Coat. Technol.*, 369 (2019) 1.
6. C. Hu, M. Xu, J. Zhang, B. Hu and G. Yu, *J. Alloys Compd.*, 770 (2019) 48.
7. S. Liu, I. Shohji, M. Iioka, A. Hashimoto, J. Hirohashi, T. Wake and S. Arai, *Applied Sciences*, 9 (2019) 1094.
8. K. Tsongas, D. Tzetzis, A. Karantzalis, G. Banias, D. Exarchos, D. Ahmadkhaniha, C. Zanella, T. Matikas and D. Bochtis, *Applied Sciences*, 9 (2019) 2901.
9. N. B. Jordanov, *Transactions of the IMF*, 97 (2019) 115.
10. H. Li, Y. He, T. He, D. Qing, F. Luo, Y. Fan and X. Chen, *J. Alloys Compd.*, 704 (2017) 32.
11. B. Li, W. Zhang, D. Li and J. Wang, *Mater. Chem. Phys.*, 229 (2019) 495.
12. B. Li, W. Zhang and D. Li, *J. Alloys Compd.*, 821 (2020) 153258.
13. W. Jiang, L. Shen, K. Wang, Z. Wang and Z. Tian, *Proceedings of the Institution of Mechanical Engineers, Part B: Journal of Engineering Manufacture*, 234 (2019) 431.
14. S. Ahmadiyeh, A. Rasooli and M. G. Hosseini, *Surf. Eng.*, 35 (2018) 861.
15. P. Jin, C. Sun, C. Zhou, L. Shi and C. Liu, *Ceram. Int.*, 45 (2019) 20155.
16. J. Zhuang, S. Lin, L. Dong, K. Cheng and W. Weng, *ACS Biomaterials Science & Engineering*, 4 (2018) 1528.
17. V. Vitry and L. Bonin, *Ultrason. Sonochem.*, 56 (2019) 327.
18. S. Taşci, R. C. Özden and M. Anik, *Metals and Materials International*, 25 (2018) 313.
19. D. Zhang, M. Qaim, W. Gao, W. Zhang, A. B. Owusu, Z. He and Y. Wang, *Materials Research Express*, 6 (2019) 126417.
20. M. Uysal, *Metallurgical and Materials Transactions A*, 50 (2019) 2331.
21. M. Karunakaran and M. Pugazh Vadivu, *J. Magn. Magn. Mater.*, 475 (2019) 359.
22. S. Sangeetha and G. P. Kalaignan, *RSC Advances*, 5 (2015) 74115.
23. S. Sangeetha and G. P. Kalaignan, *Ceram. Int.*, 41 (2015) 10415.
24. X.-H. Zhang, X.-X. Li, W.-J. Liu, Y.-Q. Fan, H. Chen and T.-X. Liang, *Rare Metals*, 38 (2018) 695.
25. C. Chen, S. Dong, R. Hou, J. Hu, P. Jiang, C. Ye, R. Du and C. Lin, *Surf. Coat. Technol.*, 326 (2017) 183.

26. B. Han and X. Lu, *Surf. Coat. Technol.*, 202 (2008) 3251.
27. C. Wang, L. Shen, M. Qiu, Z. Tian and W. Jiang, *J. Alloys Compd.*, 727 (2017) 269.
28. J. A. Cabral-Miramontes, D. M. Bastidas, M. A. Baltazar., P. Zambrano-Robledo., J. M. Bastidas, F. M. Almeraya-Calderón and C. Gaona-Tiburcio, *Int. J. Electrochem. Sci*, 15 (2019) 4226.
29. F. Xiu-qing, M. Shen, J. Lin, X.Wang and Y. Xu, *Int. J. Electrochem. Sci*, 15 (2020) 816.
30. X. Zhou and Y. Shen, *Surf. Coat. Technol.*, 235 (2013) 433.
31. A. Lelevic and F. C. Walsh, *Surf. Coat. Technol.*, 378 (2019) 124803.
32. J.-D. Lin and C.-T. Chou, *Surf. Coat. Technol.*, 368 (2019) 126.
33. M. S. Safavi, M. Fathi, S. Mirzazadeh, A. Ansarian and I. Ahadzadeh, *Surf. Eng.*, (2020) 1.
34. S. Zhong, Y. Munan, S. U. Rehman, L. Yaojun, L. Jiajie and B. Yang, *J. Alloys Compd.*, 819 (2020) 153002.
35. A. K. Chaudhari and V. B. Singh, *Arabian Journal of Chemistry*, 12 (2019) 5028.
36. Q. Y. Wang, Y. R. Tang, R. Pei, Y. C. Xi and S. Wan, *Mater. Corros.*, 71 (2019) 249.
37. Yang, Zhang, Wang, Wang, Chen, Wei and Xie, *Coatings*, 9 (2019) 758.
38. T. Xiang, M. Zhang, C. Li, C. Dong, L. Yang and W. Chan, *J. Alloys Compd.*, 736 (2018) 62.
39. M. M. Yusuf, A. B. Radwan, R. A. Shakoor, M. Awais, A. M. Abdullah, M. F. Montemor and R. Kahraman, *J. Appl. Electrochem.*, 48 (2018) 391.
40. W. Wang, Z. Chen and S. Feng, *Materials (Basel)*, 12 (2019).
41. S. Hong Zhang, M. Xi Li, J. Hong Yoon, T. Yul Cho, Y. Zhu He and C. Gyu Lee, *Sci Technol Adv Mater*, 9 (2008).
42. M. M. Abou-Krisha, A. G. Alshammari, F. H. Assaf and F. A. El-Sheref, *Arabian Journal of Chemistry*, 12 (2019) 3526.